



HAL
open science

Multifractal topography of several planetary bodies in the Solar System

François Landais, Frédéric Schmidt, Shaun Lovejoy

► **To cite this version:**

François Landais, Frédéric Schmidt, Shaun Lovejoy. Multifractal topography of several planetary bodies in the Solar System. *Icarus*, 2019, 319, pp.14 - 20. 10.1016/j.icarus.2018.07.005 . hal-01901154

HAL Id: hal-01901154

<https://hal.science/hal-01901154>

Submitted on 21 Mar 2024

HAL is a multi-disciplinary open access archive for the deposit and dissemination of scientific research documents, whether they are published or not. The documents may come from teaching and research institutions in France or abroad, or from public or private research centers.

L'archive ouverte pluridisciplinaire **HAL**, est destinée au dépôt et à la diffusion de documents scientifiques de niveau recherche, publiés ou non, émanant des établissements d'enseignement et de recherche français ou étrangers, des laboratoires publics ou privés.

Multifractal topography of several planetary bodies in the Solar System

François Landais (1), Frédéric Schmidt (1), Shaun Lovejoy (2)

May 30, 2018

(1) GEOPS, Univ. Paris-Sud, CNRS, Université Paris-Saclay, Rue du Belvédère, Bât. 504-509, 91405 Orsay, France (2) McGill University

Abstract

Topography is the expression of both internal and external processes of a planetary body. Thus hypsometry (the study of topography) is a way to decipher the dynamic of a planet. For that purpose, the statistics of height and slopes may be described by different tools, at local and global scale. We propose here to use the *multifractal* approach to describe fields of topography. This theory both encompass height and slopes and other statistical moment of the field, tacking into account the scale invariance. Contrary to the widely used *fractal* formalism, *multifractal* is able to describe the intermittency of the topography field. As we commonly observe the juxtaposition of rough and smooth at given scale, the *multifractal* framework seems to be appropriate for hypsometric studies. Here we analyze the data at global scale of the Earth, Mars, Mercury and the Moon and find that the statistics are in good agreement with the *multifractal* theory for scale larger than $\sim 10km$. Surprisingly, the analysis shows that all bodies have the same *fractal* behavior for scale smaller than $\sim 10km$. We hypothesized that dynamic topography of the mantle may be the explanation at large scale, whereas the smaller scales behavior may be related to elastic thickness.

1 Introduction

Scaling of coastlines was empirically studied by *Richardson* (1961), and *Mandelbrot* (1967) interpreted his results in terms of fractals. Fractals are geometric sets of points that have a scale symmetry. Geophysical examples of scaling include turbulent phenomena including clouds, the wind, the ocean river flows, as well as various solid earth fields including rock faults and topography. Most systems of geophysical interest are mathematical fields, not geometric sets. When scaling, they will generally be multifractals. A general way to quantify this is to determine the statistical moments of fluctuations of the field, (generalized) structure functions. Denoting the fluctuation in the topography over a distance Δx by $\Delta h(\Delta x)$, the q th order structure function is $\langle \Delta h(\Delta x)^q \rangle$. If the system is scaling, then this is a power law of the lag $\Delta x : \Delta x^{\zeta(q)}$. The field is *monofractal* if $\zeta(q) = qH$ where H is named in honour of Hurst; in this linear case the field is quasi-Gaussian. In the more general multifractal case, $\zeta(q) = qH - K(q)$ where $K(q)$ is a convex function with $K(1) = 0$, it determines the multifractality, the intermittency, the “spikeness” of the field. Numerous studies have shown that in several contexts, topography is scaling on a significant range of scales.

For multifractal processes, local estimates of fractal dimensions will be different from one location to another, they will be stochastic. It is thus possible to interpret the topography of regions with quite different slope distributions in a unified multifractal framework. This suggests that even a global analysis of the topography of a planet might be scaling and multifractal despite of its diversity and complexity. Previous studies have established that the Earth’s topography is to a good approximation multifractal over a very wide range of scales (*Lavallee et al.*, 1993; *Gagnon et al.*, 2006). In the general case, $\zeta(q)$ is a concave function; in order to characterize or model multifractals one takes advantage of the existence of stable, attractive statistical behaviour: universality classes (*Schertzer and Lovejoy*, 1987).

In a previous analysis, we performed a global analysis on the topographic MOLA data from Mars (*Smith et al.*, 2001). We also find a good agreement with universal multifractals but we found two scaling ranges with different characteristics (*Landais et al.*, 2015). The statistical structure was found to be different at small scales (nearly monofractal) and large scales (multifractal) with

a transition occurring at around $10km$. This behavior has been confirmed recently with other analyses (*Deliege et al.*, 2016).

The goal of this article is to extend this pioneering Martian work to all planetary bodies whose topography is well estimated: the Earth, the Moon and Mercury. There is topography data for Venus and Titan but unfortunately too much data is missing to have a similar analysis on the global scale.

2 Universal multifractal theory

We first define the fluctuations $\Delta h(\Delta x)$. The simplest definition is the altitude differences, the slopes multiplied by Δx , the most natural indicator of roughness. But there are many others way to define fluctuations. Wavelets provide a general method. Indeed, their coefficients define fluctuations (with appropriate normalization). The simple altitude difference corresponds to the “poor man” wavelet and can be advantageously replaced by the Haar wavelet that is more accurate and is useful over a wider range of exponents ($-1 < H < 1$, rather than $0 < H < 1$ for differences, see *Lovejoy* (2014) and paragraph below for a precise definition of Haar fluctuations.

Statistical moments We can compute any statistical moment M_q of order q define by:

$$M_q(\Delta x) = \langle \Delta h(\Delta x)^q \rangle \quad (1)$$

With $\langle \rangle$, denoting the statistical average. If $q = 2$, it simply correspond to the variance. In principle, every orders (even non-integer orders) must be computed to fully revealed the whole variability of the data. If the field is scaling, all the statistical moment are expected to follow a power-law with scale.

Multifractality Scaling allows us to introduce two distinct statistical processes : monofractal and multifractal. For a detailed description of the formalism we apply in this study, the readers can refer to *Lovejoy and Shertzer* (2013) briefly summed up in *Landais et al.* (2015) . We now quickly recall the main notions here after.

- In the usual gaussian monofractal case the parameter H is sufficient to describe the statistics of all the moments of order q (equation 2). There is no intermittency, meaning that the roughness of the field is spatially homogenous despite of its fractal variability regarding to scales. For example, the value $H = 0.5$ corresponds to the classic Brownian motion. This kind of statistical object has proved to be relevant in many local and regional analysis of natural surfaces (*Orosei et al.*, 2003; *Rosenburg et al.*, 2011), at least on restricted ranges of scales but fails to give full account to the intermittency commonly observed on larger topographic datasets.

$$M_q \sim \Delta x^{qH} \quad (2)$$

- In the multifractal case, H is no more sufficient to fully describe the statistics of the moments of order q . An additional convex function $K(q)$ depending on q is required (see eq. 3). The moment scaling function K slightly modifies the scaling law of each moment. The consequence on the corresponding field appears clearly on simulations (*Gagnon et al.*, 2006) : the field exhibits a juxtaposition of rough and smooth places that are clearly more realistic in the case of natural surfaces. Moreover, it is possible to restrain the generality of the function $K(q)$, considering only universal multifractals, a stable and attractive class proposed by *Schertzer and Lovejoy* (1987) for which the multifractality is completely determined by the mean intermittency $C_1 = \left(\frac{dK(q)}{dq} \right)_{q=1}$ (codimension of the mean) and the curvature α of the function K , $\alpha = \frac{1}{C_1} \frac{d^2K(q)}{dq^2}$ (the degree of multifractality). In that case the expression of K is simply given by equation 5.

$$M_q \sim \Delta x^{qH - K(q)} \quad (3)$$

$$\xi(q) = qH - K(q) \quad (4)$$

$$K(q) = \frac{C_1}{\alpha - 1} (q^\alpha - q) \quad (5)$$

We see that the monofractal case corresponds to $(H \neq 0, C_1 = 0)$ or $(H \neq 0, C_1 \neq 0, \alpha \rightarrow 0)$.

3 Dataset

The topography of a planet is defined as the difference between the distance of the planetary surface and the geoid. For Mars (*Smith et al.*, 2001), Mercury (*Cavanaugh et al.*, 2007) and the Moon (*Smith et al.*, 2010), we are used topographic data stored in PDS (<http://pds-geosciences.wustl.edu>) whereas the Earth data (*Amante and Eakins*, 2009) are gathered from numerous global and regional data sets. Table 1 sums up the main characteristics of the datasets. Each has already been previously analysed.

The Earth has been studied for multifractal purpose by *Gagnon et al.* (2006) using ETOPO5 dataset. They proposes to analyse separately continents and ocean and found that H is varying from 0.46 for bathymetry and 0.66 for continent. The dataset considered in our study (ETOPO1, *Amante and Eakins*, 2009) is an arc-minute global relief model of the Earth.

On Mars, the main source of topographic data is the Laser altimeter MOLA (*Smith et al.*, 2001) that allowed to perform extensive statistical analysis with different roughness indicators on sliding windows revealing interesting correlation with geological units (*Aharonson et al.*, 2001; *Kreslavsky and Head*, 2000). The monofractal scaling of the topography of Mars has also been studied by *Orosei et al.* (2003) through the local computation of the scale independent Hurst parameters revealing a high disparity of values across the martian surfaces as expected for multifractal topography.

On the Moon, the high-precision topographic data obtained by the laser altimeter LOLA (*Smith et al.*, 2010) has been extensively used. *Kreslavsky et al.* (2013) computed maps of roughness at hectometer and kilometer scales revealing poor correlations between these two scales. Moreover, *Rosenburg et al.* (2011) measured H . They not only identified a transition that occurs around 1km at most location but they also found significantly different values of H in the Highlands ($H = 0.95$) and in the Marias ($H = 0.76$).

On Mercury, by using the MLA data (*Cavanaugh et al.*, 2007), *Pommerol et al.* (2012) computed roughness indicators on extracted profiles from geologically distinct regions. Due to the eccentricity of the orbit, only the northern hemisphere could be mapped by laser altimetry with a resolution of about 5 kilometers. The use of pairs of stereoscopic images has finally made possible to develop an overall map of the topography of Mercury (*Solomon et al.*, 2001; *Hawkins et al.*, 2007). We

analyzed both MLA data only and the full map (from both laser and stereoscopy) and found no significant difference, except the fact that larger scale are available for the full map. We thus choose to present here the full map only. This result confirm that there is no significant bias (at least with on multifractal properties) between stereoscopic and laser altimetric techniques.

The current study proposes to extend the scope of the multifractal analysis already performed on Earth and Mars (*Gagnon et al.*, 2006; *Landais et al.*, 2015) to all the bodies in the solar system for data is adequate . Thus the case of Earth, Mars, Moon and Mercury will be comparatively discussed. The case of Venus is not considered here despite of the existence of a dataset collected by Magellan because of the relative lack of topographic data comparing to the other bodies (*Ford et al.*, 2014). The case is equivalent for Titan (*Stiles et al.*, 2009).

4 Methodology

In our previous analysis (*Landais et al.*, 2015), we considered the 1-D topographic profiles directly extracted from the along-track measurement of MOLA stored in PDS (<http://pds-geosciences.wustl.edu>, *Smith et al.* 2001). As the data are irregularly sampled due to the presence of clouds and instrument problems, we used multifractal simulations to study the effect of a MOLA-like irregular signal on the Haar fluctuations . It turned out that, most probably due to the small fraction of missing data, the irregularity had no detectable impact on the analysis. We also found that the use of the gridded data also produced the same results has the direct use of the more reliable along-track measurement, the conclusion being that for the purpose of a global analysis, the extrapolated gridded map for each body is sufficient to recover the global statistical parameters. The methodology used here is therefore much simpler and only relies on the gridded data . We only considered 1D

	source	radius (km)	Resolution	min scale	max scale	lines	columns	nb fluctuations
Earth	ETOPO1	6371	60 pix/deg	1 853 m	20 015 km	10 800	21 600	0.2 billions
Mars	MOLA	3390	128 pix/deg	462 m	10 650 km	22 528	46 080	1 billion
Moon	LOLA	1737	512 pix/deg	60m	5 457 km	92 160	184 320	13 billions
Mercury	MLA	2240	64 pix/deg	665 m	7 037 km	11 520	23 040	0.0002 billion

Table 1 – Characteristics of the datasets

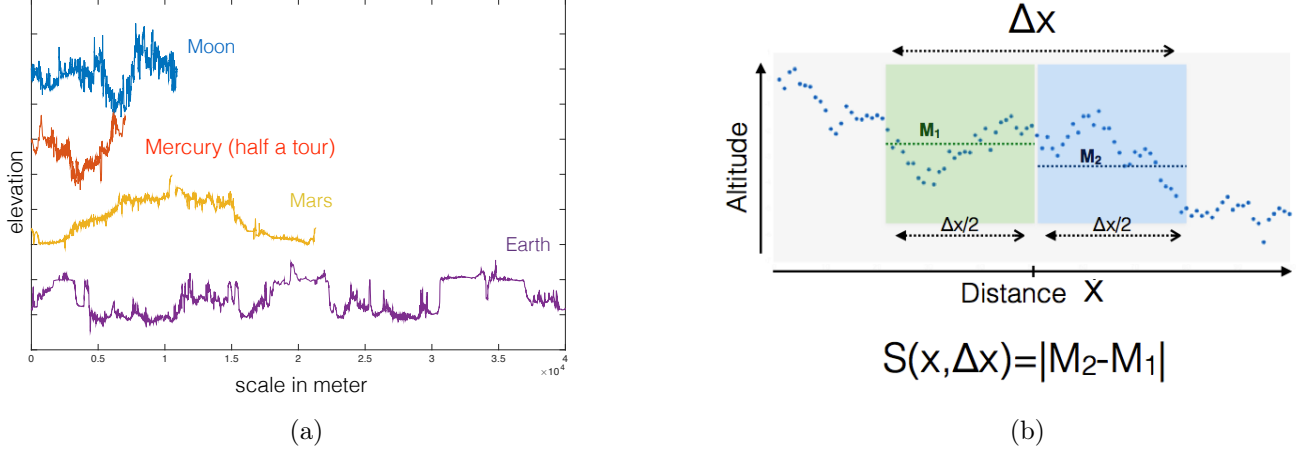


Figure 1 – (a) Topographic dataset: 4 typical profiles, 1 for each body in the scope of this study. The length corresponds to 1 complete circumference of the planets except in the case of Mercury (only half a circumference) (b) Definition of the Haar fluctuation used to perform the statistical analysis. M_1 (respectively M_2) is the average of the first half (respectively second half) of the topographic profile.

North-South profiles and computed the Haar fluctuations at different lags Δx . The simplification to 1-D is reasonable as we perform a global statistical analysis. In addition, the North/South direction is more relevant than East-West because each profile as the same length. Figure 1a provides an example of 1-D profiles extracted from the gridded field for each body. See *Landais et al. (2015)* for a review of the different biases that could result from such an approach.

We implicitly consider that the global statistic are isotropic. This assumption is reasonable for the purpose of a global analysis given the fact that shape of various orientation can be found on a given body. Although local anisotropy is commonly observed (*Kreslavsky and Head, 2003; Bondarenko et al., 2006; Bills et al., 2014*), we assume it is erased by the spatial averaging. Isotropic multifractal processes readily produce strong local anisotropy so that the question of systematic scale dependant statistical anisotropy is not easy to establish. Anisotropy remains an important issue and will be more carefully considered in future works

Haar fluctuation and statistical moments At a given location x and a given scale Δx corresponding to N successive elevation data on the grid, we average separately the first $\frac{N}{2}$ points $M_1(x, \Delta x)$ and last $\frac{N}{2}$ points $M_2(x, \Delta x)$. The Haar fluctuation is simply defined as the difference $S(x, \Delta x) = |M_2(x, \Delta x) - M_1(x, \Delta x)|$. This definition is illustrated by figure 1b. The Mean Haar

Fluctuation (MHF , moment of order 1) is simply obtained by averaging all the available haar fluctuations in a dataset. By extension, other statistical moments of any order q , $M_{q,HF}$ may be computed by averaging the fluctuations raised to the power of q :

$$MHF = \langle S(x, \Delta x) \rangle$$

$$MHF_q = \langle S(x, \Delta x)^q \rangle$$

5 Results for Earth, Mars, Mercury and the Moon

Mean Haar Fluctuations (MHF) Figure 2 shows the Mean Haar Fluctuations (MHF , moment of order 1) for each body on a log-log plot. One can observe its scaling behavior as a function of the real distance (in meters). One can observe that at small scale, MHF is from the larger to the smaller for : the Moon, Mercury, Mars, the Earth. This simply means that statistically, the roughness is from the larger to the smaller: for the Moon, Mercury, Mars, the Earth. Thus a astronaut (coming from the Earth) would experience topography differently by looking at the landscape of other planetary bodies. He would feel smaller in front of a rougher landscape at his/her scale. This feeling should be larger for the Moon. Another interesting features is the resemblance between i) the curves of Earth and Mars and ii) the curves the Moon and Mercury. For the two small bodies, the MHF is clearly above the two others, except at the highest scales. By interpreting it as a roughness indicator, this feature simply reflects the well-known high level of roughness of small bodies, a consequence of intense craterisation shaping their surfaces.

As expected, the global MHF increases with scale in all cases, simply reflecting the fact that larger scales yield larger differences in elevation. Nevertheless for the Earth and Mercury, at large scales, the MHF begins to decrease before reaching its maximum scale. More specifically, as our goal is to study the global scaling behavior of topography, we expect this global increase of the MHF to be linear on a log-log plot. It is clearly not the case on the entire available range of scales. Still noticeable scaling appears but over restricted ranges of scale : a transition seems to

occur, separating two distinct scaling regimes. Such a transition is observed for all the bodies and interestingly, it occurs around 10-20 km in each case including the Moon. The nature of this transition discussed in our previous analysis focused on Mars and already pointed out by other authors in the case of Mars (*Malamud and Turcotte, 2001*), remains unknown.

On Figure 3, the MHF are normalized by their respective values around 10 km in order to emphasize the transition at that scale. As one can see, the slope at small scales ($< 10km$) are rather similar ($H \sim 0.8$) whereas significantly different slopes are observed at large scales ($H \sim 0.2-0.5$). The scaling is excellent at large scales in the case of Mars and good in the case of Earth and Mercury. In the case of the Moon, data points are more dispersed, and H might be less well defined. Note also at small scales, the available range for Earth and Mercury is limited and might result in an unconvincing fit. The values obtained for H for each body by computing a linear regression on the distinct ranges of scale is reported on table 2.

Statistical moments MHF_q In the case of universal multifractals, all the statistical moment will scale according to equation 3, the MHF being the particular case for which $q = 1$. Thus we can estimate the other multifractal exponents by computing statistical moments MHF_q . On Figure 4, the MHF_q are plotted for different values of q and for the different bodies. The next step is to compute linear regressions on every curve and on the distinct identified scaling regime. The log-log slopes $\zeta(q)$ may then be plotted as a function of q for each body and for each range of scale (see Figure 5) in order to visualize the function ξ defined by equation 4. A linear $\xi(q)$ is the signature of monofractality whereas a curved $\xi(q)$ indicates a multifractal behavior according to equation 2 and 3. Interestingly, Figure 5 clearly shows that on the distinct scaling regimes (low scale and large scales) the behavior is significantly different. On the range of small scales ($< 10km$, plot on the left), the curves are rather similar for all the four bodies and very close to straight lines indicating that the statistics found to be roughly monofractal (small C_1) over the range. Over the range of large scales ($> 10km$, plot on the right), we obtained curved structure functions in most cases revealing the multifractal nature of the statistics of topography over the range. The multifractal parameters are computed according to equation 3 and reported on table 2. Whereas the case of Mars, Mercury and Earth are similar of value of C_1 around 0.1, the case of the moon

seems to be an exception with weak multifractal properties over that range of scales (C_1 close to 0).

6 Discussion and conclusion

By averaging the fluctuations at different scales, we have revealed global statistical pattern of planetary bodies. We tested and validated the multifractal approach on the four bodies with empirically well estimated topography : the Earth, Mars, Mercury and the Moon. We found that a transition occurs at about 10 km and that it is a general property of all planetary topographies. Below 10 km, differences in altitudes decrease more rapidly when the scale decreases.

As suggested by *Araki et al.* (2009) and *Nimmo et al.* (2011), for the transition in the power spectral density, we propose the interpretation that the elastic thickness of the lithosphere is responsible for this transition by acting against the deformations caused by the different surface processes in two regimes. At scales smaller than the elastic thickness T_e , a modification of the surface (for example, following an impact) does not make it possible to generate isostatic compensation. The new relief can therefore remain present. The slopes of neighboring facets tend to be correlated with each other and give rise to fluctuations in topography rapidly increasing with the scale (structured aspect, high H). The relief profile tends to be constructive since the slopes are highly correlated. At scales higher than T_e , a change in relief triggers an isostatic compensation which tends to oppose the large variations of the relief. The slopes of neighboring facets tend to be anti-correlated and the

scale<10km	Earth	Mars	Moon	Mercury
H	0.823 ± 0.004	0.773 ± 0.003	0.878 ± 0.002	0.922 ± 0.003
α	NA	NA	NA	NA
C_1	0.01 ± 0.01	0.02 ± 0.006	0.02 ± 0.04	0.026 ± 0.005
scale>10km	Earth	Mars	Moon	Mercury
H	0.479 ± 0.001	0.53 ± 0.001	0.226 ± 0.002	0.248 ± 0.002
α	1.70 ± 0.08	1.80 ± 0.06	1.4 ± 0.1	1.85 ± 0.1
C_1	0.093 ± 0.002	0.110 ± 0.002	0.03 ± 0.01	0.059 ± 0.002

Table 2 – Estimations of multifractal parameters. NA stands for non-applicable. If the value of C_1 is very small (here <0.02), we can consider that the field is not multifractal and the value of α is not interpretable.

topographic profile is rougher. The relief oscillates around a mean value since the slope are more anti-correlated. In this configuration, the altitude fluctuations increase only slightly regarding to scale (low H). The common transition could be explained by the averaged value of the elastic thickness quite similar for the 5 bodies (*Grott and Breuer, 2008; Barnett et al., 2000; Nimmo and Watters, 2004*).

At scales larger than 10 km, all planetary bodies are different. Interestingly, the scaling law is characterized for the Moon by $H = 0.2$, Mercury by $H = 0.3$, Mars and Earth by $H = 0.5$. The smaller the body, the less intense its internal activity due to intense thermal cooling. The value of H may be related to its geological activity. One can speculate that a more intensively convecting mantle yields a higher value of H . This explanation links the large scale with dynamic topography (*Hager et al., 1985*). The fact that only large scale topography is strongly multifractal is coherent with this explanation because multifractal behavior is related to fluids mechanics and turbulent scale cascade. The geological origin of this transition will be investigated in future works.

From our result, this pattern seems coherent on large ranges of scale throughout the different bodies. Although suggesting that a few processes might operate simultaneously at different scales, this result is not incompatible with the existence of process operating at a specific altitude or locations. For example the “glacial buzz” saw effect seems limit the presence of high altitude on the Earth only (*Lorenz et al., 2011*). Our results simply suggest that the contribution of such process to global statistics can be neglected because if a strong altitude dependent process occurs, it should have broken the scaling behavior.

As a future work, we plan to perform local analysis on area defined by geological boundaries or altitude level to better understand the link between the scaling behavior of topography and natural processes operating at different location and altitude.

Acknowledgment

We acknowledge support from the “Institut National des Sciences de l’Univers” (INSU), the "Centre National de la Recherche Scientifique" (CNRS) and "Centre National d’Etudes Spatiales" (CNES). This work was supported by the Programme National de Planétologie (PNP) of CNRS/INSU, co-

funded by CNES

References

- Aharonson, O., M. T. Zuber, and D. H. Rothman (2001), Statistics of mars' topography from the mars orbiter laser altimeter: Slopes, correlations, and physical models, *Journal of Geophysical Research: Planets*, 106(E10), 23,723–23,735, doi:10.1029/2000JE001403.
- Amante, C., and B. Eakins (2009), Etopo1 1 arc-minute global relief model: Procedures, data sources and analysis., *NOAA Technical Memorandum NESDIS NGDC-24. National Geophysical Data Center, NOAA*.
- Araki, H., et al. (2009), Lunar global shape and polar topography derived from kaguya-lalt laser altimetry, *Science*, 323(5916), 897–900.
- Barnett, D. N., F. Nimmo, and D. McKenzie (2000), Elastic thickness estimates for venus using line of sight accelerations from magellan cycle 5, *Icarus*, 146(2), 404–419.
- Bills, B. G., S. W. Asmar, A. S. Konopliv, R. S. Park, and C. A. Raymond (2014), Harmonic and statistical analyses of the gravity and topography of vesta, *Icarus*, 240, 161–173.
- Bondarenko, N., M. Kreslavsky, and J. Head (2006), North-south roughness anisotropy on venus from the magellan radar altimeter: Correlation with geology, *Journal of Geophysical Research: Planets*, 111(E6).
- Cavanaugh, J. F., et al. (2007), *The Mercury Laser Altimeter Instrument for the MESSENGER Mission*, pp. 451–479, Springer New York, New York, NY.
- Deliege, A., T. Kleyntssens, and S. Nicolay (2016), *The Fractal Nature of Mars Topography Analyzed via the Wavelet Leaders Method*, pp. 1295–1298, Springer International Publishing, Cham.
- Fernando, J., F. Schmidt, X. Ceamanos, P. Pinet, S. Douté, and Y. Daydou (2013), Surface CO₂reflectance of CO₂Mars observed by CRISM/MRO: 2. Estimation of surface photometric

- properties in Gusev Crater and Meridiani Planum, *Journal of Geophysical Research (Planets)*, *118*, 534–559, doi:10.1029/2012JE004194.
- Ford, P., F. Pettengill, G. Liu, and Q. J. (2014), Magellan global topography 4641m, *PDS Geo-Science Node*.
- Gagnon, J.-S., S. Lovejoy, and D. Schertzer (2006), Multifractal earth topography, *Nonlinear Processes in Geophysics*, *13*(5), 541–570, doi:10.5194/npg-13-541-2006.
- Grott, M., and D. Breuer (2008), The evolution of the martian elastic lithosphere and implications for crustal and mantle rheology, *Icarus*, *193*(2), 503–515.
- Hager, B. H., R. W. Clayton, M. A. Richards, R. P. Comer, and A. M. Dziewonski (1985), Lower mantle heterogeneity, dynamic topography and the geoid, *Nature*, *313*(6003), 541–545.
- Hawkins, S. E., et al. (2007), The mercury dual imaging system on the messenger spacecraft, *Space Science Reviews*, *131*(1), 247–338.
- Kreslavsky, M., and J. Head (2003), North–south topographic slope asymmetry on mars: Evidence for insolation-related erosion at high obliquity, *Geophysical Research Letters*, *30*(15).
- Kreslavsky, M. A., and J. W. Head (2000), Kilometer-scale roughness of mars: Results from mola data analysis, *Journal of Geophysical Research: Planets*, *105*(E11), 26,695–26,711, doi:10.1029/2000JE001259.
- Kreslavsky, M. A., J. W. Head, G. A. Neumann, M. A. Rosenburg, O. Aharonson, D. E. Smith, and M. T. Zuber (2013), Lunar topographic roughness maps from lunar orbiter laser altimeter (lola) data: Scale dependence and correlation with geologic features and units, *Icarus*, *226*(1), 52 – 66, doi:http://dx.doi.org/10.1016/j.icarus.2013.04.027.
- Landais, F., F. Schmidt, and S. Lovejoy (2015), Universal multifractal martian topography, *Non-linear Processes in Geophysics*, *22*(6), 713–722, doi:10.5194/npg-22-713-2015.

- Lavallee, D., S. Lovejoy, D. Schertzer, and P. Ladoy (1993), Nonlinear variability and landscape topography: analysis and simulation. fractals in geography, *Eds. L. De Cola, N. Lam, 158-192, PTR, Prentice Hall.*
- Lorenz, R. D., E. P. Turtle, B. Stiles, A. Le Gall, A. Hayes, O. Aharonson, C. A. Wood, E. Stofan, and R. Kirk (2011), Hypsometry of titan, *Icarus, 211(1)*, 699–706.
- Lovejoy, S. (2014), A voyage through scales, a missing quadrillion and why the climate is not what you expect, *Climate Dynamics.*
- Lovejoy, S., and D. Shertzer (2013), *The Weather and Climate :Emergent Laws and Multifractal Cascades*, Cambridge.
- Malamud, B. D., and D. L. Turcotte (2001), Wavelet analyses of mars polar topography, *Journal of Geophysical Research: Planets, 106(E8)*, 17,497–17,504, doi:10.1029/2000JE001333.
- Mandelbrot, B. (1967), How long is the coast of britain? statistical self-similarity and fractional dimension, *Science, 156(3775)*, 636–638, doi:10.1126/science.156.3775.636.
- Mosegaard, K., and A. Tarantola (1995), Monte carlo sampling of solutions to inverse problems, *Journal of Geophysical Research: Solid Earth, 100(B7)*, 12,431–12,447.
- Nimmo, F., and T. Watters (2004), Depth of faulting on mercury: Implications for heat flux and crustal and effective elastic thickness, *Geophysical research letters, 31(2)*.
- Nimmo, F., B. Bills, and P. Thomas (2011), Geophysical implications of the long-wavelength topography of the saturnian satellites, *Journal of Geophysical Research: Planets, 116(E11)*.
- Orosei, R., R. Bianchi, A. Coradini, S. Espinasse, C. Federico, A. Ferriccioni, and A. I. Gavrishin (2003), Self-affine behavior of martian topography at kilometer scale from mars orbiter laser altimeter data, *Journal of Geophysical Research: Planets, 108(E4)*, n/a–n/a, doi: 10.1029/2002JE001883.
- Pommerol, A., S. Chakraborty, and N. Thomas (2012), Comparative study of the surface roughness of the moon, mars and mercury, *Planetary and Space Science, 73*, 287–293.

- Richardson, L. F. (1961), The problem of contiguity: An appendix to statistic of deadly quarrels, *General systems : yearbook of the Society for the Advancement of General Systems Theory*, 61, 139–187.
- Rosenburg, M. A., O. Aharonson, J. W. Head, M. A. Kreslavsky, E. Mazarico, G. A. Neumann, D. E. Smith, M. H. Torrence, and M. T. Zuber (2011), Global surface slopes and roughness of the moon from the lunar orbiter laser altimeter, *Journal of Geophysical Research: Planets*, 116(E2), n/a–n/a, doi:10.1029/2010JE003716.
- Schertzer, D., and S. Lovejoy (1987), Physical modeling and analysis of rain and clouds by anisotropic scaling multiplicative processes, *Journal of Geophysical Research: Atmospheres*, 92(D8), 9693–9714, doi:10.1029/JD092iD08p09693.
- Schmidt, F., and J. Fernando (2015), Realistic uncertainties on hapke model parameters from photometric measurement, *Icarus*, 260, 73–93.
- Smith, D. E., et al. (2001), Mars orbiter laser altimeter: Experiment summary after the first year of global mapping of mars, *Journal of Geophysical Research: Planets*, 106(E10), 23,689–23,722, doi:10.1029/2000JE001364.
- Smith, D. E., et al. (2010), The lunar orbiter laser altimeter investigation on the lunar reconnaissance orbiter mission, *Space Science Reviews*, 150(1), 209–241, doi:10.1007/s11214-009-9512-y.
- Solomon, S. C., et al. (2001), The messenger mission to mercury: Scientific objectives and implementation, *Planetary and Space Science*, 49(14), 1445–1465.
- Stiles, B. W., et al. (2009), Determining titan surface topography from cassini {SAR} data, *Icarus*, 202(2), 584 – 598, doi:http://doi.org/10.1016/j.icarus.2009.03.032.
- Tarantola, A., and B. Valette (1982), Generalized nonlinear inverse problems solved using the least squares criterion, *Reviews of Geophysics*, 20(2), 219–232.

Annex : Bayesian regression

In order to estimate the best set of parameters (H, C_1, α) modeling the data, the parameters can be estimated in a classical way by performing regressions on the function ζ near the mean ($q = 1$) to quantify its curvature related to α and C_1 *Lovejoy and Shertzer (2013)* by the theoretical formulas:

$$H = \left. \frac{d\xi(q)}{dq} \right|_{q=1} \quad C_1 = \left. \frac{dK(q)}{dq} \right|_{q=1} \quad \alpha = -2 \left. \frac{d^2K(q)}{dq^2} \right|_{q=1} / \left. \frac{dK(q)}{dq} \right|_{q=1} \quad (6)$$

As a reminder, the scaling exponents $\zeta(q)$ are themselves the products of linear regression, so the fits from eq. 6 are only indirectly related the data. We wish to avoid this method which will not make possible to judge the quality of the estimates, especially as the multifractal component is rather weak when the function $\zeta(q)$ is only weakly curved.

We propose a new approach based on principle of Bayesian inversion (*Tarantola and Valette, 1982*) which allows to construct a posterior probability distribution of the parameters (mean, most probable value, standard deviation) from observations. In practice, these distributions can be estimated iteratively by applying the Metropolis rule to construct a Monte Carlo Markov chain (*Mosegaard and Tarantola, 1995*) containing the different sets of parameters. We summarize the main lines of this technique, already used on photometry problems (*Schmidt and Fernando, 2015; Fernando et al., 2013*). As a first step, it is necessary to evaluate the quality of the individual linear regressions of each moment. In this step, we attribute to each point an empirical uncertainty with a centered gaussian distribution. The latter will be the higher as the linear correlation through the scale is accurate. Then, we tested the direct model, computed by applying the laws of equations 4 and 4, for different random set of parameters (H, C_1, α) . Synthetic realizations are then compared to observations. The Monte Carlo Markov chain is created according the metropolis rules, using the likelihood of empirical uncertainties. . This method allow us to estimated realistic uncertainty bars on parameter (H, C_1, α) , from the observational data (see table 2)

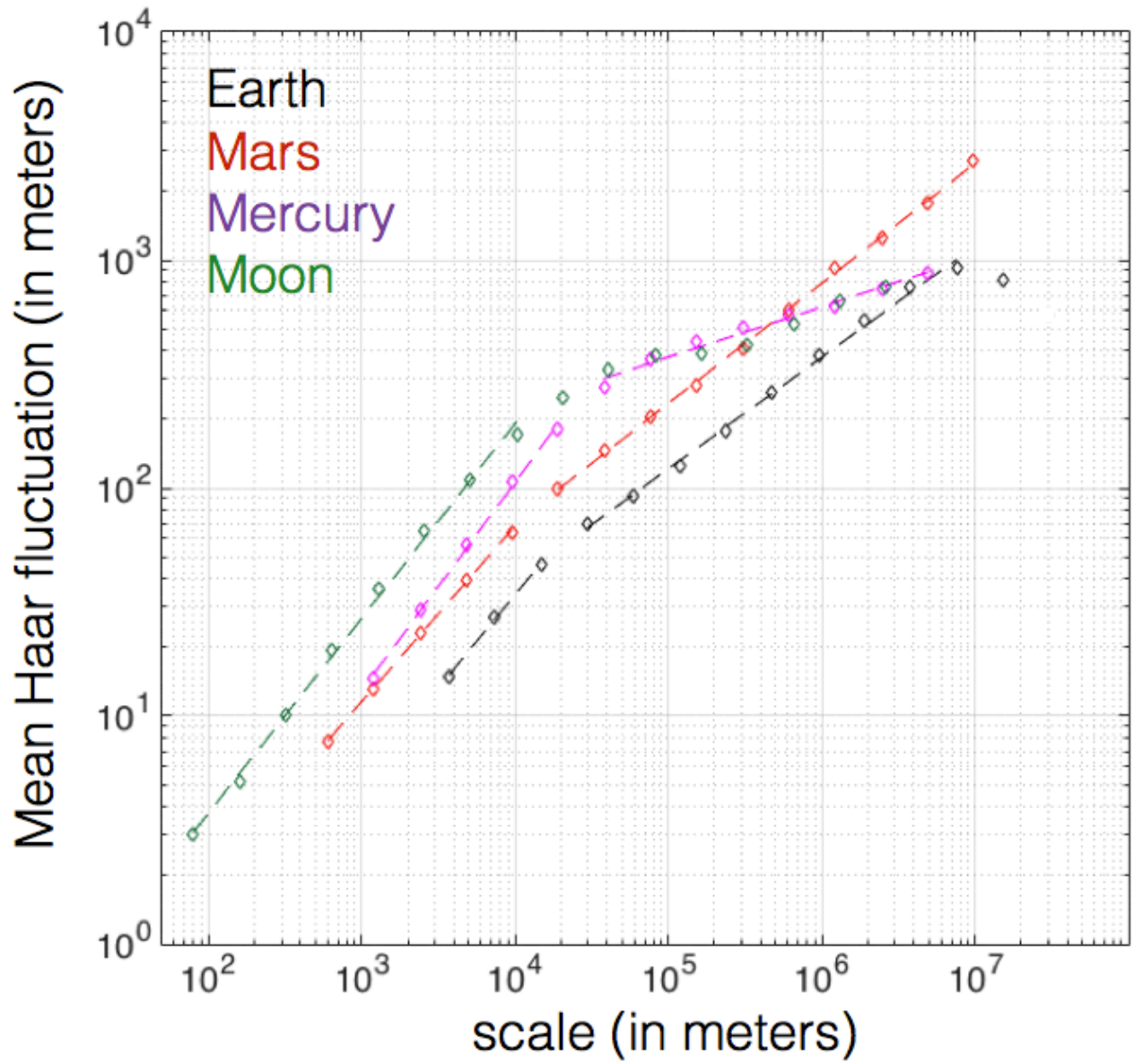


Figure 2 – Mean Haar fluctuations MHQ (order 1) as a function of scales for the 4 planetary bodies.

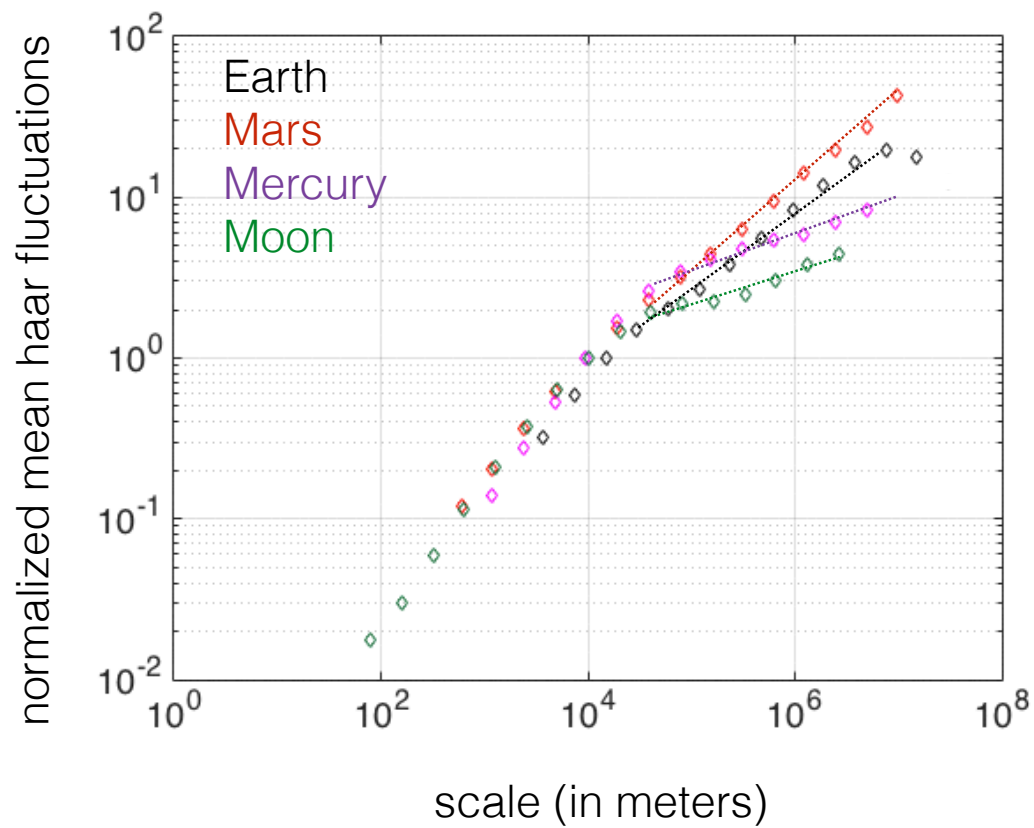


Figure 3 – Mean Haar fluctuations normalized in order to be approximately equal at scale 10km, as a function of scale. The normalization does not modify the scaling behavior from Fig. 2 but

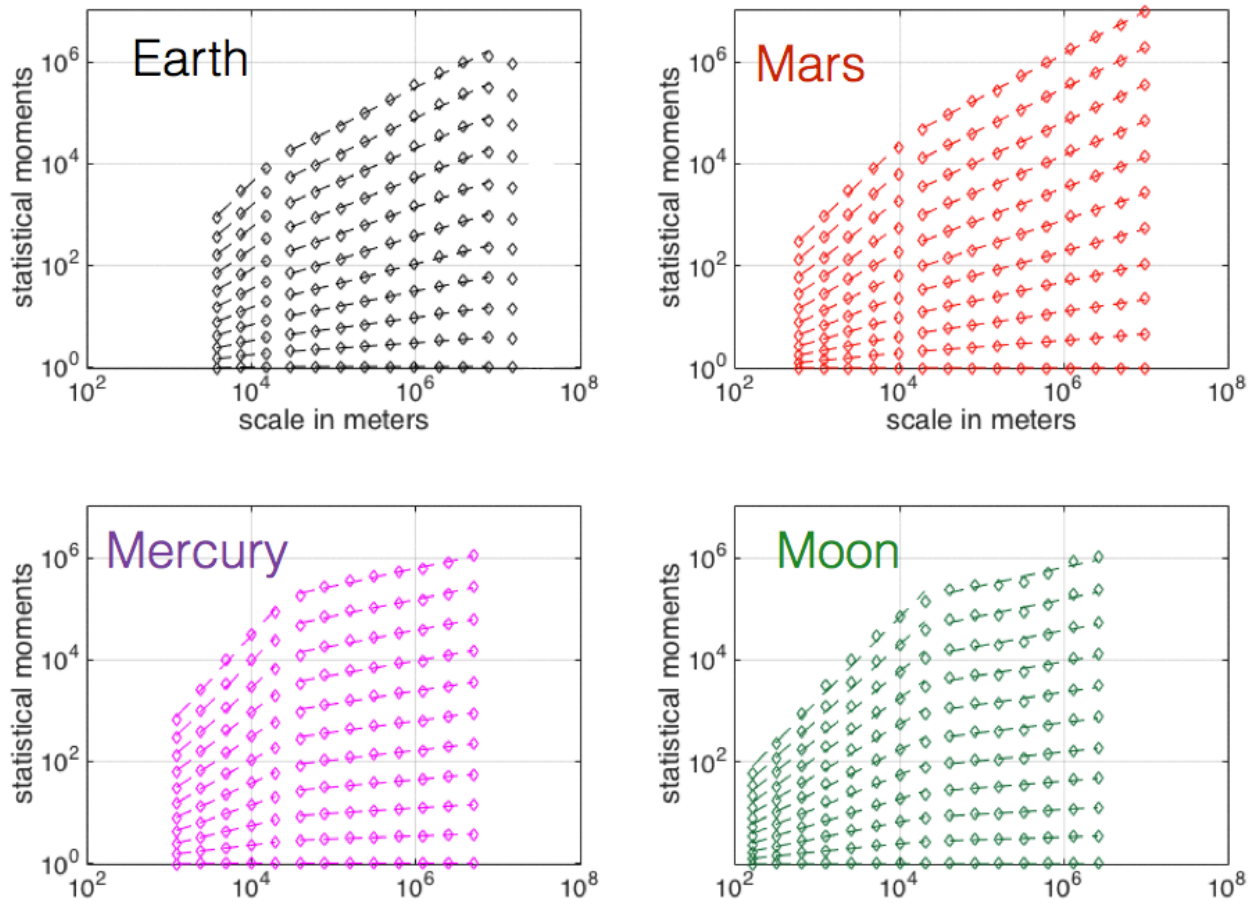


Figure 4 – Plot of different statistical moments for the four bodies. The average fluctuations from figure 2 are shown as diamond whereas the moments of order 2 (average squared fluctuations) are triangles (top curves). In between are the non-integer order statistical moments. Although 21 moments have been computed for the purpose of this analysis (from 0.1 to 2 by steps of 0.1), only a few non-integers moments are plotted here for order 0.1 to order 2 by step of 0.2

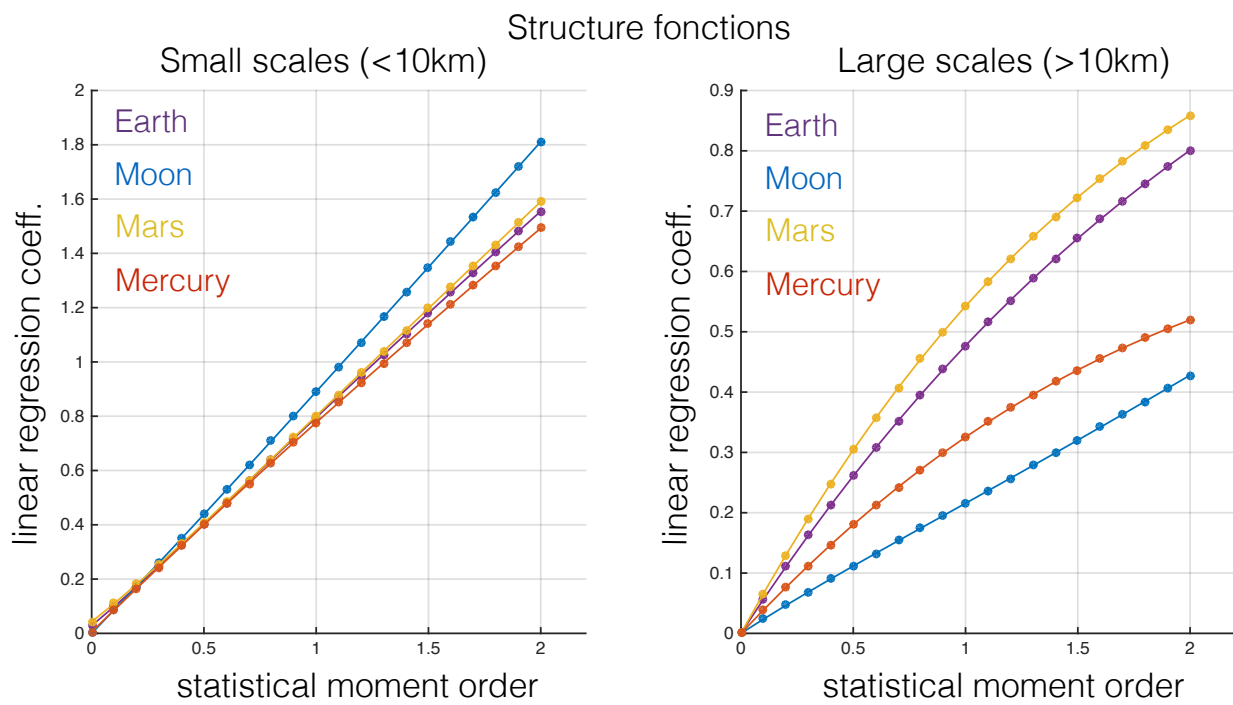


Figure 5 – Structure function for different ranges of scales